A high-order finite volume method for hyperbolic systems: Multi-dimensional Optimal Order Detection (MOOD).

Stéphane Clain, Steven Diot, Raphaël Loubère

HAL Id: hal-00518478

https://hal.archives-ouvertes.fr/hal-00518478v2

Submitted on 15 Feb 2011

A high-order finite volume method for systems of conservation laws — Multi-dimensional Optimal Order Detection (MOOD).

S. Clain [a,b], S. Diot [a], R. Loubère [a]

[a] *Institut de Mathématiques de Toulouse, Université de Toulouse, France*

[b] *Departamento de Matemática e Aplicações Campus de Gualtar - 4710-057 Braga Campus de Azurm - 4800-058 Guimares, Portugal*

Abstract

In this paper, we investigate an original way to deal with the problems generated by the limitation process of high-order finite volume methods based on polynomial reconstructions. Multi-dimensional Optimal Order Detection (MOOD) breaks away from classical limitations employed in high-order methods. The proposed method consists of detecting problematic situations after each time update of the solution and of reducing the local polynomial degree before recomputing the solution. As multi-dimensional MUSCL methods, the concept is simple and independent of mesh structure. Moreover MOOD is able to take physical constraints such as density and pressure positivity into account through an "a posteriori" detection. Numerical results on classical and demanding test cases for advection and Euler system are presented on quadrangular meshes to support the promising potential of this approach.

Key words: Finite Volume, high-order, conservation law, MUSCL, polynomial reconstruction, limitation, MOOD.

Email addresses: `stephane.clain@math.univ-toulouse.fr` (S. Clain), `steven.diot@math.univ-toulouse.fr` (S. Diot), `raphael.loubere@math.univ-toulouse.fr` (R. Loubère).

1 Introduction

High-order methods for systems of nonlinear conservation laws are an important challenging question with a wide range of applications. Furthermore in an engineering context such methods may deal with complex multi-dimensional domains requiring unstructured, heterogeneous or even non-conformal meshes. To handle highly stretched unstructured meshes made with different cell shapes, one has to design genuinely multi-dimensional numerical methods which exclude dimensional splitting techniques.

Due to its simplicity (one unknown mean value per cell) and built-in conservativity property, first-order finite volume method is very popular in today's engineering applications or commercial codes. However, it suffers from a major drawback, namely the presence of a large amount of numerical diffusion leading to a poor accuracy and over smoothed discontinuities. High-order space and time finite volume methods based on local polynomial reconstructions and Runge-Kunta algorithm have been developed to improve the approximation accuracy. MUSCL methods are probably the most popular second-order finite volume schemes. First developed in the one-dimensional situation with linear reconstructions [14,27,15,16], the technique has been extended to genuinely multi-dimensional case using structured or unstructured meshes [3,2,12,20,7,21,4]. Stability is achieved using a limiting procedure based on the Maximum Principle. In the present study, the Multi-dimensional Limiting Process (MLP) of [20,21] is employed since it is one of the most up-to-date MUSCL methods. Besides, (Weighted) Essentially Non Oscillatory polynomial reconstruction procedures (ENO/WENO) were designed to reach higher-order of accuracy [10,11,1,24,23] using less restrictive conditions for the limitation which do not guarantee a strict Maximum Principle for scalar problems. Moreover, although ENO/WENO schemes can retain high-order spatial accuracy even at points of extrema, extra difficulties and complexities have to be faced for the implementation on multi-dimensional unstructured grids (see [1,28]) as a large number of stencils for the polynomial reconstructions must be proceeded. Such drawbacks lead us to put ENO/WENO methods aside from the present study.

In this work we propose a genuinely multi-dimensional high-order method within a finite volume Eulerian framework on non-uniform meshes, the Multi-dimensional Optimal Order Detection (MOOD) method. In contrast to the traditional methods which use an *a priori* limitation procedure, the MOOD technique is based on an *a posteriori* detection of problematic cells. In each cell optimal polynomial degrees are determined to build approximated states leading to a discrete maximum principle preserving solution. In an hydrodynamics context, physical properties such as the density and the pressure positivity are considered. Roughly speaking, the polynomial degree may drop to zero in the vicinity of discontinuities leading to a local stable first-order finite volume scheme whereas high-order scheme is achieved in smooth regions.

2

As for other methods, the MOOD method is embedded into the sub-steps of a high-order Runge-Kutta time discretization.

The paper is organized as follows. Section 2 is dedicated to the generic framework used to describe the MOOD method. Section 3 is devoted to the linear reconstruction and to a short presentation of the MLP method [20,21]. The MOOD method for scalar problems is detailed in the fourth section while section 5 is dedicated to an extension of MOOD method to the Euler equations. At last, the numerical results for the advection and the Euler equations problems are respectively gathered in sections 6 and 7. Classical tests are carried out and comparisons to the results of MLP method are provided. Several numerical examples prove the efficiency of the MOOD method in its second- and third-order version. The last section finally gathers conclusion and perspectives.

2 General framework

We consider the generic scalar hyperbolic equation defined on a domain $\Omega \subset \mathbb{R}^2$, $t > 0$ cast in the conservative form

$$\partial_t u + \nabla \cdot F(u) = 0, \tag{1a}$$
$$u(\cdot, 0) = u_0, \tag{1b}$$

where $u = u(\mathbf{x}, t)$ is the unknown function, $\mathbf{x} = (x_1, x_2)$ denotes a point of Ω and t the time. F is the physical flux and u_0 is the initial condition. Boundary conditions shall be prescribed in the following.

To elaborate the discretization in space and time, we introduce the following ingredients. We assume that the computation domain Ω is a polygonal bounded set of $\mathbb{R}^2$ divided into quadrangles K_i, $i \in \mathcal{E}_{el}$ where $\mathcal{E}_{el}$ is the cell index set with $\mathbf{c_i}$ being the cell centroid. For each cell K_i, $\lambda(i)$ is the set of all the nodes P_m, $m \in \lambda(i)$ while e_{ij} denotes the common edge between K_i and K_j with $j \in \underline{\nu}(i)$, $\underline{\nu}(i)$ being the index set of all the elements which share a common side with K_i. Moreover, $\overline{\nu}(i)$ represents the index set of all K_j such that $K_i \cap K_j \neq \emptyset$ (see figure 1). At last, $|K_i|$ and $|e_{ij}|$ measure the surface of K_i and the length of e_{ij} respectively and $\mathbf{n}_{ij}$ is the unit outward normal vector of K_i.

To compute an approximation of the solution of equation (1), we recall the generic first-order explicit finite volume scheme

$$u_i^{n+1} = u_i^n - \Delta t \sum_{j \in \underline{\nu}(i)} \frac{|e_{ij}|}{|K_i|} \, \mathbb{F}(u_i^n, u_j^n, \mathbf{n}_{ij}), \tag{2}$$
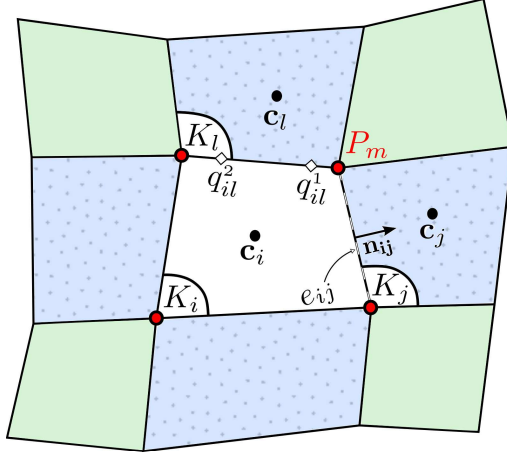
3

Fig. 1. Mesh notation. K_i is a generic element with the centroid $\mathbf{c_i}$. Index set $\underline{\nu}(i)$ corresponds to blue cells with dots, $\overline{\nu}(i)$ corresponds to every non-white cells and $\lambda(i)$ is the set of red P_m node indexes. Edges are denoted by e_{ij} with $\mathbf{n}_{ij}$ the unit outward normal vector of element K_i. Numerical integration on edge e_{il} is performed with the two Gauss points q_{il}^1, q_{il}^2.

where $\mathbb{F}(u_i^n, u_j^n, \mathbf{n}_{ij})$ is a numerical flux which satisfies the classical properties of consistency and monotonicity.

Unfortunately, such a scheme only provides first-order accuracy in space and higher-order reconstruction techniques are used to improve the solution approximation. To this end, we substitute in equation (2) the first-order approximation u_i^n and u_j^n with better approximations of u on the e_{ij} edge and consider the generic spatial high-order finite volume scheme

$$u_i^{n+1} = u_i^n - \Delta t \sum_{j \in \underline{\nu}(i)} \frac{|e_{ij}|}{|K_i|} \sum_{r=1}^R \xi_r \mathbb{F}(u_{ij,r}^n, u_{ji,r}^n, \mathbf{n}_{ij}), \tag{3}$$

where $u_{ij,r}^n$ and $u_{ji,r}^n$, $r = 1, ..., R$ are high-order representations of u on both sides of edge e_{ij} and ξ_r denote the quadrature weights for the numerical integration. In practice, $u_{ij,r}^n$ and $u_{ji,r}^n$ are two approximations of $u(q_{ij}^r, t^n)$ at quadrature points $q_{ij}^r \in e_{ij}$, $r = 1, ..., R$ (see figure 1).

For the sake of simplicity, let us write the scheme under the compact form

$$u_h^{n+1} = u_h^n + \Delta t\, \mathcal{H}^R(u_h^n), \tag{4}$$

with $u_h^n = \sum_{i \in \mathcal{E}_{el}} u_i^n \mathbb{I}_{K_i}$ the constant piecewise approximation of function u and operator $\mathcal{H}^R$ being defined as

$$\mathcal{H}^R(u_h^n) := \sum_{i \in \mathcal{E}_{el}} \left(- \sum_{j \in \underline{\nu}(i)} \frac{|e_{ij}|}{|K_i|} \sum_{r=1}^R \xi_r \mathbb{F}(u_{ij,r}^n, u_{ji,r}^n, \mathbf{n}_{ij}) \right) \mathbb{I}_{K_i}. \tag{5}$$

4

To provide a high-order method in time, we use the third-order TVD Runge-Kutta method (see [24]) which corresponds to a convex combination of three explicit steps

$$u_h^{(1)} = u_h^n + \Delta t \, \mathcal{H}^R \left(u_h^n \right), \tag{6a}$$

$$u_h^{(2)} = u_h^{(1)} + \Delta t \, \mathcal{H}^R(u_h^{(1)}), \tag{6b}$$

$$u_h^{(3)} = \left(\frac{3u_h^n + u_h^{(2)}}{4} \right) + \Delta t \, \mathcal{H}^R \left(\frac{3u_h^n + u_h^{(2)}}{4} \right), \tag{6c}$$

$$u_h^{n+1} = \frac{u_h^n + 2u_h^{(3)}}{3}. \tag{6d}$$

Remark 1 *Note that a high-order scheme in space and time can be rewritten as convex combinations of the first-order scheme. From a practical point of view, implementation of the high-order scheme from an initial first-order scheme is then straightforward.* □

The main challenge is to build the approximations $u_{ij,r}^n$ and $u_{ji,r}^n$ on both sides of edge e_{ij} with $r = 1, ..., R$ to be plugged into relations (5) and (6). Polynomial reconstructions provide high-order approximations but unphysical oscillations arise in the vicinity of discontinuities. Indeed, the exact solution of an autonomous scalar conservation law (1) satisfies a local Maximum Principle and we intend to build the reconstructions such that this stability property is fulfilled at the numerical level (see [5,6] and references herein). To this end, we state the following definition.

Definition 2 *A numerical scheme (4) satisfies the Discrete Maximum Principle (DMP) if for any cell index $i \in \mathcal{E}_{el}$ one has*

$$\min_{j \in \overline{\nu}(i)} (u_i^n, u_j^n) \leq u_i^{n+1} \leq \max_{j \in \overline{\nu}(i)} (u_i^n, u_j^n). \tag{7}$$

3 A short review on a multi-dimensional MUSCL method

All L^∞ stable second-order schemes are based on piecewise linear reconstructions equipped with a limiting procedure. The polynomial reconstruction provides the accuracy while the limitation algorithm ensures the physical relevancy of the numerical approximation. We briefly present the piecewise linear reconstruction step and recall the MLP method proposed in [21] which is used in the numerical part of this paper.

5

3.1 Linear reconstruction

Let $(u_i)_{i \in \mathcal{E}_{el}}$ be a set of cell centered mean values given on cells K_i. In order to simplify notations, let K be a generic cell with centroid $\mathbf{c} = (c_1, c_2)$. Considering mean values on a chosen neighborhood made of cells K_j, $j \in \nu$, we seek a polynomial function $\widetilde{u}(\mathbf{x})$ of degree $d = 1$. Let us define the notation for the mean value as

$$\left\langle \widetilde{u}(\mathbf{x}) \right\rangle_K \overset{\text{def}}{=} \frac{1}{|K|} \int_K \widetilde{u}(\mathbf{x}) d\mathbf{x}.$$

Usually we ask for the following criteria

Criterion 3 *The polynomial reconstruction $\widetilde{u}$ must fulfill*

(1) $\left\langle \widetilde{u}(\mathbf{x}) \right\rangle_K = \bar{u}$ *where $\bar{u}$ is the mean value approximation of u on K.*
(2) The polynomial coefficients are the ones minimizing the functional

$$E(\widetilde{u}) = \sum_{j \in \nu} \left(u_j - \left\langle \widetilde{u}(\mathbf{x}) \right\rangle_{K_j} \right)^2, \tag{8}$$

A classic way to write $\widetilde{u}$ is

$$\widetilde{u}(\mathbf{x}) = \bar{u} + G \cdot (\mathbf{x} - \mathbf{c}), \tag{9}$$

where $G = (G_1, G_2)$ is a constant approximation of ∇u on K. The first condition of criterion 3 is directly satisfied and classical techniques like least squares methods are used to determine vector G that minimizes the functional E in equation (8) .

3.2 Gradient limitation

As we mentioned above, a finite volume scheme only based on a local polynomial reconstruction without limiting procedure produces spurious oscillations. Initiated by the pioneer works of Kolgan and Van Leer [14,15,27,16], the MUSCL technique deals with a local linear reconstruction like (9) on each cell K where the gradient G is reduced by a limiter coefficient $\phi \in [0, 1]$

$$\widetilde{u}(\mathbf{x}) = \bar{u} + \phi \left(G \cdot (\mathbf{x} - \mathbf{c}) \right). \tag{10}$$

such that any reconstructed values satisfy the Discrete Maximum Principle (see [2,3,12]). We choose to detail and use the MLP limiter instead of the classical Barth-Jespersen limiter because it provides more accurate results (see [21]). The MLP limiter applies the following procedure.

- Construction of an unlimited slope G using the neighbor cells K_j, $j \in \overline{\nu}$.
- Evaluation of the unlimited reconstruction (9) at the vertices P_m of K: $u_m = \widetilde{u}(P_m)$, $m \in \lambda$ the nodes index set of K.
- Evaluation of the bounds for each node P_m

$$\delta u_m^{\max} = \max_{j,\, P_m \in \lambda(j)} (u_j - \bar{u}), \quad \delta u_m^{\min} = \min_{j,\, P_m \in \lambda(j)} (u_j - \bar{u}).$$

- Evaluation of the vertex based limiter ϕ_m

$$\phi_m = \begin{cases} \min\left(1, \dfrac{\delta u_m^{\max}}{u_m - \bar{u}}\right) & \text{if } u_m - \bar{u} > 0, \\[2ex] \min\left(1, \dfrac{\delta u_m^{\min}}{u_m - \bar{u}}\right) & \text{if } u_m - \bar{u} < 0, \\[2ex] 1 & \text{if } u_m - \bar{u} = 0. \end{cases}$$

- Cell-centered limiter $\phi = \min_{m \in \lambda} \phi_m$.

The MLP technique provides a second-order finite volume scheme which satisfies the Discrete Maximum Principle under a more restrictive CFL condition than the CFL condition of the first-order scheme.

Remark 4 *Although there exists a large literature about piecewise linear limitation, the extension of MUSCL type methods to piecewise quadratic or even higher degree polynomials in a multi-dimensional context is not yet achieved. An efficient limitation process is still an under-investigation field of research.* □

4 The Multi-dimensional Optimal Order Detection method (MOOD)

Classical high-order methods are based on an *a priori* limitation of the reconstructed values which are plugged into a one time step generic finite volume scheme to update the mean values (see figure 2 top).
Unlike existing methods, the MOOD technique proceeds with an *a posteriori* limitation. Over each cell, an unlimited polynomial reconstruction is carried out to build a prediction $u_h^\star$ of the updated solution. Then the *a posteriori* limitation consists of reducing the polynomial degree and recomputing the predicted solution $u_h^\star$ until the DMP property (7) is achieved. To this end, a prescribed maximum degree $d_{\max}$ is introduced and used to perform an initial polynomial reconstruction on each cell. Through an iterative decremental procedure, we determine the *optimal degree* $\mathsf{d}_i \leq d_{\max}$ on each cell K_i such that each updated mean value $u_i^\star$ fulfills the DMP property (see figure 2 bottom).

In the following we focus on the quadratic polynomial case $d_{\max} = 2$ and first
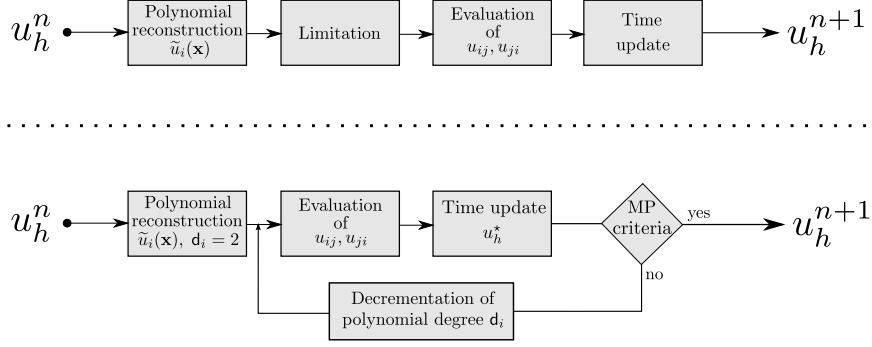
Fig. 2. Classical high-order methods idea (top) and MOOD idea (bottom).

present the local quadratic reconstruction of [19]. Then the MOOD method is detailed and we prove that the numerical approximations satisfy the DMP property.

4.1 Quadratic reconstruction

Using the same framework as in section 3.1, the quadratic polynomial reconstruction is written

$$\widetilde{u}(\mathbf{x}) = \bar{u} + G \cdot (\mathbf{x} - \mathbf{c}) + \frac{1}{2}\left((\mathbf{x} - \mathbf{c})^t H(\mathbf{x} - \mathbf{c}) - \bar{H}\right), \qquad (11)$$

with

$$\bar{H} = \left\langle (\mathbf{x} - \mathbf{c})^t H(\mathbf{x} - \mathbf{c}) \right\rangle_K, \qquad H = \begin{bmatrix} H_{11} & H_{12} \\ H_{12} & H_{22} \end{bmatrix},$$

where matrix H is an approximation of the Hessian matrix $\nabla^2 u$ on K. Note that by construction, the mean value of $\widetilde{u}$ on K is still equal to $\bar{u}$.

A minimization technique is used to compute G and H. To this end, for a cell K_j, let us define the integrals

$$\mathbf{x}_{K_j}^{\{\alpha,\beta\}} = \left\langle (x - c_1)^\alpha (y - c_2)^\beta \right\rangle_{K_j} - \left\langle (x - c_1)^\alpha (y - c_2)^\beta \right\rangle_K.$$

Algebraic manipulations yield the following expression for $\left\langle \widetilde{u}(\mathbf{x}) \right\rangle_{K_j}$

$$\left\langle \widetilde{u}(\mathbf{x}) \right\rangle_{K_j} = \bar{u} + \left(G_1\, \mathbf{x}_{K_j}^{\{1,0\}} + G_2\, \mathbf{x}_{K_j}^{\{0,1\}}\right) + \frac{1}{2}\left(H_{11}\mathbf{x}_{K_j}^{\{2,0\}} + 2H_{12}\mathbf{x}_{K_j}^{\{1,1\}} + H_{22}\mathbf{x}_{K_j}^{\{0,2\}}\right).$$

$$(12)$$

8

This expression is further derived for any cell K_j with $j \in \nu$ to form an over-determined linear system of the form $A\Lambda = B$ with

$$
A = \begin{pmatrix} \mathbf{x}_{K_1}^{\{1,0\}} & \mathbf{x}_{K_1}^{\{0,1\}} & \mathbf{x}_{K_1}^{\{2,0\}} & \mathbf{x}_{K_1}^{\{1,1\}} & \mathbf{x}_{K_1}^{\{0,2\}} \\ \mathbf{x}_{K_2}^{\{1,0\}} & \mathbf{x}_{K_2}^{\{0,1\}} & \mathbf{x}_{K_2}^{\{2,0\}} & \mathbf{x}_{K_2}^{\{1,1\}} & \mathbf{x}_{K_2}^{\{0,2\}} \\ \vdots & \vdots & \vdots & \vdots & \vdots \\ \mathbf{x}_{K_N}^{\{1,0\}} & \mathbf{x}_{K_N}^{\{0,1\}} & \mathbf{x}_{K_N}^{\{2,0\}} & \mathbf{x}_{K_N}^{\{1,1\}} & \mathbf{x}_{K_N}^{\{0,2\}} \end{pmatrix}, \ \Lambda = \begin{pmatrix} G_1 \\ G_2 \\ \frac{1}{2}H_{11} \\ H_{12} \\ \frac{1}{2}H_{22} \end{pmatrix}, \ B = \begin{pmatrix} u_1 - \bar{u} \\ u_2 - \bar{u} \\ \vdots \\ u_N - \bar{u} \end{pmatrix},
$$

(13)

with $N = \#\nu$. This system is solved with a QR decomposition of A using Householder transformations, such that $Q \in \mathcal{M}_{N \times N}(\mathbb{R})$ is an orthogonal matrix and $R \in \mathcal{M}_{N \times 5}(\mathbb{R})$ an upper-triangular one. Finally back-substitution of $R\Lambda = Q^t B$ defines $\widetilde{u}$ (see [19]).

Remark 5 *A left preconditioner matrix can be applied to reduce the system sensitivity and improve the reconstruction quality. For example, in [19], the authors use a diagonal matrix whose coefficients $\omega_{jj} = \|\mathbf{c_j} - \mathbf{c}\|^{-2}$ ($j = 1, \ldots, N$) correspond to geometrical weights in order to promote closest informations.* □

4.2 Description of the MOOD method

We now detail the MOOD technique considering the simple case where an explicit time discretization is employed. Moreover, without loss of generality, we present the method using only one quadrature point ($R = 1$) and skip the subscript r denoting u_{ij} in place of $u_{ij,r}$. Extension to several quadrature points ($R > 1$) is straightforward.

Assume that we have a given sequence $u_h^n = (u_i^n)_{i \in \mathcal{E}_{el}}$ of mean value approximations at time t^n, the goal is to build a relevant sequence $u_h^{n+1} = (u_i^{n+1})_{i \in \mathcal{E}_{el}}$ at time $t^{n+1} = t^n + \Delta t$. To this end, we define the following fundamental notions.

- d_i is the Cell Polynomial Degree (CellPD) which represents the degree of the polynomial reconstruction on cell K_i.
- d_{ij} and d_{ji} are the Edge Polynomial Degrees (EdgePD) which correspond to the effective degrees used to respectively build u_{ij} and u_{ji} on both sides of edge e_{ij}.

The MOOD method consists of the following iterative procedure.

1. **CellPD initialization.** Each CellPD is initialized to d_{max}.

2. **EdgePD evaluation.** Each EdgePD is set up as a function of the neighboring CellPD (see table 1).
3. **Quadrature points evaluation.** Each u_{ij} is evaluated with the polynomial reconstruction of degree d_{ij}.
4. **Mean values update.** The updated values $u_h^\star$ are computed using the finite volume scheme (3).
5. **DMP test.** The DMP criterion is checked on each cell K_i

$$\min_{j \in \overline{\nu}(i)} (u_i^n, u_j^n) \leq u_i^\star \leq \max_{j \in \overline{\nu}(i)} (u_i^n, u_j^n). \tag{14}$$

If $u_i^\star$ does not satisfy (14) the CellPD is decremented, $\mathsf{d}_i := \max(0, \mathsf{d}_i - 1)$.
6. **Stopping criterion.** If all cells satisfy the DMP property, the iterative procedure stops with $u_h^{n+1} = u_h^\star$ else go to step 2.

We give in table 1 three possible strategies of EdgePD calculation. The simplest one named EPD_0 consists of setting $\mathsf{d}_{ij} = \mathsf{d}_i$ and $\mathsf{d}_{ji} = \mathsf{d}_j$ whereas EPD_1 chooses the minimal value between d_i and d_j for both d_{ij} and d_{ji}. At last, the smallest CellPD of all the direct neighbor cells is taken in the EPD_2 strategy.

To conclude the section, there are two important remarks which dramatically reduce the computational cost.

Remark 6 *If $\mathsf{d}_{ij} < d_{max}$, there is no need to recompute a polynomial of degree d_{ij}, a simple truncation of the initial polynomial of degree d_{max} should be performed.* □

Remark 7 *Only cells K_i where CellPD has been decremented and their neighbors in a compact stencil have to be updated. Consequently only these cells have to be checked during next iterations of the MOOD procedure in the current*

	EPD$_0$ strategy	EPD$_1$ strategy	EPD$_2$ strategy
EdgePD d_{ij}	d_i	$\min(\mathsf{d}_i, \mathsf{d}_j)$	$\displaystyle\min_{j \in \underline{\nu}(i)} (\mathsf{d}_i, \mathsf{d}_j)$
Example			

Table 1

Evaluation of the EdgePD d_{ij} using the CellPD of the two neighbor elements. Analytic formula on first line. Examples on the second line where CellPD are surrounded in red and EdgePD for internal edges are in black. Missing cells are assumed to have CellPD equal to 2.

10

time step. For instance the compact stencil for EPD_0 *and* EPD_1 *is* $\underline{\nu}(i)$ *while for* EPD_2 *it is* $\left\{ \underline{\nu}(i) \cup \{\underline{\nu}(j), j \in \underline{\nu}(i)\} \right\}$. $\quad\square$

4.3   Convergence of the MOOD method

We first recall the classical stability result (see [6] and references herein).

Proposition 8 *Let us consider the generic first-order finite volume scheme (2) with reflective boundary conditions. If the numerical flux is consistent and monotone, then the DMP property given by definition 2 is satisfied.*

It implies that if $u_{ij} = u_i$ and $u_{ji} = u_j$ for all $j \in \underline{\nu}(i)$ then relation (7) holds. To prove that the iterative MOOD method provides a solution which satisfies the DMP, we introduce the following definition.

Definition 9 *An* EPD *strategy is said upper-limiting (with respect to the* CellPD*) if for any* K_i

$$\mathsf{d}_i = \bar{\mathsf{d}} \implies \mathsf{d}_{ij} \leq \bar{\mathsf{d}} \; \text{ and } \; \mathsf{d}_{ji} \leq \bar{\mathsf{d}}, \quad \forall j \in \underline{\nu}(i). \tag{15}$$

We then have the following theorem.

Theorem 10 *Let us consider the generic high-order finite volume scheme with reflective boundary conditions and assume that the numerical flux is consistent and monotone. If the* EPD *strategy is upper-limiting then the MOOD method provides an updated solution* u_h^{n+1} *which satisfies the DMP property after a finite number of iterations.*

PROOF. Let d_i be the CellPD of cell K_i. If $\mathsf{d}_i = 0$, then equation (15) implies that $\mathsf{d}_{ij} = \mathsf{d}_{ji} = 0$, hence $u_{ij}^n = u_i^n$ and $u_{ji}^n = u_j^n$, for all $j \in \underline{\nu}(i)$. We recover the first-order scheme (2) and proposition 8 yields that u_i^{n+1} satisfies the DMP property (7). Otherwise, if $\mathsf{d}_i > 0$ then two situations arise. Either the Maximum principle is satisfied and we do not modify d_i or we decrement d_i. Consequently if the maximum principle is not satisfied for all cells, then there is at least one cell having its CellPD positive which has to be decremented. Since we can not decrement more than $d_{\max} \times \#(\mathcal{E}_{el})$ times, the iterative procedure stops after a finite number of iterations and the solution satisfies the DMP property. $\quad\square$

Remark 11 *Note that* EPD_1 *and* EPD_2 *are upper-limiting strategies whereas* EPD_0 *strategy does not satisfy condition (15). Thus* EPD_0 *cannot be used since MOOD iterative procedure may loop endlessly.* $\quad\square$

Remark 12 *To carry out a third-order Runge-Kutta time discretization (6)*

which provides a solution satisfying the DMP property, one has to perform the MOOD technique for each explicit sub-step since (6) can be written as a convex combination. □

5 Extension to the Euler Equations

In this section, we propose an extension of the MOOD method to the Euler equations.

$$\partial_t \begin{pmatrix} \rho \\ \rho u_1 \\ \rho u_2 \\ E \end{pmatrix} + \partial_{x_1} \begin{pmatrix} \rho u_1 \\ \rho u_1^2 + p \\ \rho u_1 u_2 \\ u_1(E + p) \end{pmatrix} + \partial_{x_2} \begin{pmatrix} \rho u_2 \\ \rho u_1 u_2 \\ \rho u_2^2 + p \\ u_2(E + p) \end{pmatrix} = 0, \qquad (16)$$

where ρ, $\mathbf{V} = (u_1, u_2)$ and p are the density, velocity and pressure respectively while the total energy per unit volume E is given by

$$E = \rho \left(\frac{1}{2} \mathbf{V}^2 + e \right), \quad \mathbf{V}^2 = u_1^2 + u_2^2,$$

where e is the specific internal energy. For an ideal gas, this system is closed by the equation of state

$$e = \frac{p}{\rho(\gamma - 1)},$$

with γ the ratio of specific heats.

Despite that the physical variables do not have to respect the maximum principle, classical methods such as the MUSCL technique use a limiting procedure derived from the scalar case to keep the numerical solution from producing spurious oscillations. A popular choice consists of reconstructing and limiting the density, the velocity components and the pressure variables but other limitations can be carried out: the internal energy, the specific volume or the characteristic variables for instance.

Although applying the MOOD technique to each variable independently gives physically admissible solutions, an excessive diffusion is noticed. We thus propose a strategy to both have an accurate approximation where the solution is smooth and prevent the oscillations from appearing close to the discontinuities. In the following we consider ρ, u_1, u_2 and p as the variables to be reconstructed.

First we have to provide physically relevant reconstructed values at quadrature points, and since no limitation is used in the MOOD method, negative reconstructed values for pressure or density must be avoided (it would be the

12

same for energy or specific volume). In that case, first-order values are substituted to the unphysical reconstructed values, for instance if the reconstructed value ρ_{ij} is negative on cell K_i, we replace it with the mean value ρ_i.

We now describe how we choose to use the two fundamental notions of the MOOD method (CellPD and EdgePD) in the Euler equations framework. Instead of using one CellPD per cell and per variable, we choose to define only one CellPD per cell and to use it for all variables. Consequently only one EdgePD is defined per side of an edge and used for all variables.

As in the scalar case, we first build the local polynomial reconstruction of maximal degree $d_{\max}$ for each variable. Then we apply the MOOD algorithm of Section 4.2 where we substitute steps 5 and 6 with the following stages.

5. **Density DMP test.** The DMP criterion is checked on the density

$$\min_{j \in \overline{\nu}(i)} (\rho_i^n, \rho_j^n) \leq \rho_i^\star \leq \max_{j \in \overline{\nu}(i)} (\rho_i^n, \rho_j^n). \tag{17}$$

   If $\rho_i^\star$ does not satisfy (17) the CellPD is decremented, $d_i := \max(0, d_i - 1)$.

6. **Pressure positivity test.** The pressure positivity is checked and if $p_i^\star \leq 0$ and d_i has not been altered by step 5 then the CellPD is decremented, $d_i := \max(0, d_i - 1)$.

7. **Stopping criterion.** If, for all $i \in \mathcal{E}_{el}$, d_i has not been altered by steps 5 and 6 then the iterative procedure stops and returns $u_h^{n+1} = u_h^\star$ else go to step 2.

Next section is dedicated to numerical experiments to assess the computational efficiency of the MOOD method.

6 Numerical results — the scalar case

Let Ω be the unit square $[0,1] \times [0,1]$. We first consider the linear advection problem of a scalar quantity u with velocity $V(\mathbf{x})$:

$$\partial_t u + \nabla.(Vu) = 0, \tag{18a}$$
$$u(.,0) = u^0, \tag{18b}$$

where $V(\mathbf{x})$ is a given continuous function on Ω and u^0 is the initial function we shall characterize in the following. In this section periodic boundary conditions are prescribed on $\partial\Omega$.

Comparisons are drawn between the simple first-order Finite Volume method (denoted FV with an abuse of terminology), the MUSCL method proposed in [21] (MLP) and the MOOD method with $d_{\max} = 1$ (MOOD-P1) and $d_{\max} = 2$

(MOOD-P2).

We use the following monotone upwind numerical flux (see equation (2))

$$\mathbb{F}(u_i^n, u_j^n, \mathbf{n}_{ij}) = [V(\mathbf{x}) \cdot \mathbf{n}_{ij}]^+ u_i^n + [V(\mathbf{x}) \cdot \mathbf{n}_{ij}]^- u_j^n,$$

where the velocity is evaluated at the quadrature point $\mathbf{x}$ and the positive and negative parts are respectively defined by

$$[\alpha]^+ = \max(0, \alpha) \quad \text{and} \quad [\alpha]^- = \min(0, \alpha).$$

Notice that we use $\overline{\nu}(i)$ as the reconstruction stencil. Lastly two Gauss points are used on each edge to provide a third-order accurate spatial integration while time integration is performed with a forward Euler scheme for the FV method and with the RK3-TVD method given by system (6) for the MLP and MOOD methods.

Following remark 12, we simply apply the MOOD procedure detailed in section 4.2 to each sub-step of the RK3-TVD. The CellPD are thus reinitialized to $d_{\max}$ at the beginning of each time sub-step.

6.1 Test descriptions

The method accuracy is measured using L^1 and L^∞ errors which are computed with

$$err_1 = \sum_{i \in \mathcal{E}_{el}} |u_i^N - u_i^0||K_i| \quad \text{and} \quad err_\infty = \max_{i \in \mathcal{E}_{el}} |u_i^N - u_i^0|,$$

where $(u_i^0)_i$ and $(u_i^N)_i$ are respectively the cell mean values at initial time $t = 0$ and final time $t = t_f = N\Delta t$.

Two classical numerical experiments are carried out to demonstrate the ability of the method to provide effective third-order accuracy and to handle discontinuities with a very low numerical diffusion.

Double Sine Translation (DST)

We consider a constant velocity $V = (2, 1)$ and the initial condition is the C^∞ function

$$u^0(x_1, x_2) = \sin(2\pi x_1) \sin(2\pi x_2).$$

The final time is $t_f = 2.0$. Since we use periodic boundary conditions, the final time corresponds to a full revolution such that the exact solution coincides with the initial one.

Solid Body Rotation(SBR)

First introduced by R.J. Leveque in [17], this solid body rotation test uses three shapes which are a hump, a cone and a slotted cylinder. Each shape is located within a circle of radius $r^0 = 0.15$ and centered at (x_1^0, y_2^0)

14

Hump centered at $(x_1^0, x_2^0) = (0.25, 0.5)$

$$u^0(x_1, x_2) = \frac{1}{4}(1 + \cos(\pi \min(r(x_1, x_2), 1))).$$

Cone centered at $(x_1^0, x_2^0) = (0.5, 0.25)$

$$u^0(x_1, x_2) = 1 - r(x_1, x_2).$$

Slotted cylinder centered at $(x_1^0, x_2^0) = (0.5, 0.75)$

$$u^0(x_1, x_2) = \begin{cases} 1 & \text{if } |x_1 - 0.5| < 0.25, \text{ or } x_2 > 0.85, \\ 0 & \text{elsewhere,} \end{cases}$$

where $r(x_1, x_2) = \frac{1}{r^0}\sqrt{(x_1 - x_1^0)^2 + (x_2 - x_2^0)^2}$. To perform the rotation, we use the velocity $V(\mathbf{x}) = (-x_2 + 0.5, x_1 - 0.5)$ and the final time $t_f = 2\pi$ corresponds to one full rotation.

6.2 Numerical results

6.2.1 Comparison between EPD_1 and EPD_2 strategies

We consider the DST test case on uniform meshes from 20×20 to 160×160 cells and compare the L^1 and L^∞ errors and convergence rates displayed in table 2 using EPD_1 and EPD_2 strategies with the MOOD-P2 method. We obtain an almost effective third-order convergence in L^1 norm and a 1.6 convergence rate in L^∞ norm for the two strategies. We observe in this case that the L^1 and L^∞ errors for EPD_1 are slightly less important than for EPD_2 and the convergence orders seem to indicate that the EPD_1 strategy should be privileged. Moreover, from a practical point of view, the EPD_1 implementation is performed with a more compact stencil than the EPD_2 (see remark 7). In the sequel, only EPD_1 strategy is used.

6.2.2 Comparison between FV, MLP, MOOD-P1 and MOOD-P2 with EPD_1 strategy on uniform meshes

Double Sine Translation. We report in table 3, 4 and 5 the L^1 and L^∞ errors and convergence rates for FV, MLP, MOOD-P1, MOOD-P2, unlimited P1 and P2 reconstruction methods respectively. At last, we plot in figure 3 the convergence curves for the four methods as well as the convergence curves for the unlimited versions.

15

Table 2

L^1 and L^∞ errors and convergence rates for DST problem with the MOOD-P2 method: EPD_1 strategy (left) and EPD_2 strategy (right).

Nb of	EPD_1				EPD_2			
Cells	err_1		err_∞		err_1		err_∞	
20x20	9.469E-02	—	3.960E-01	—	1.104E-01	—	4.506E-01	—
40x40	1.113E-02	3.09	1.333E-01	1.57	1.382E-02	3.00	1.566E-01	1.52
80x80	1.768E-03	2.65	4.164E-02	1.68	2.309E-03	2.58	5.196E-02	1.59
160x160	2.481E-04	2.83	1.304E-02	1.68	3.262E-04	2.82	1.698E-02	1.61

Table 3

L^1 and L^∞ errors and convergence rates for the DST on uniform meshes with FV and MLP methods.

Nb of	FV				MLP			
Cells	err_1		err_∞		err_1		err_∞	
20x20	3.924E-01	—	9.371E-01	—	1.417E-01	—	3.765E-01	—
40x40	3.480E-01	0.17	8.375E-01	0.16	3.038E-02	2.22	1.121E-01	1.75
80x80	2.663E-01	0.39	6.241E-01	0.42	6.904E-03	2.14	3.534E-02	1.67
160x160	1.734E-01	0.62	3.964E-01	0.65	1.693E-03	2.03	1.167E-02	1.60

Table 4

L^1 and L^∞ errors and convergence rates for the DST on uniform meshes with MOOD-P1 and MOOD-P2 methods.

Nb of	MOOD-P1				MOOD-P2			
Cells	err_1		err_∞		err_1		err_∞	
20x20	1.502E-01	—	4.876E-01	—	9.469E-02	—	3.960E-01	—
40x40	3.141E-02	2.26	1.629E-01	1.58	1.113E-02	3.09	1.333E-01	1.57
80x80	7.438E-03	2.08	5.188E-02	1.65	1.768E-03	2.65	4.164E-02	1.68
160x160	1.787E-03	2.06	1.675E-02	1.63	2.481E-04	2.83	1.304E-02	1.68

The high-order finite volume methods with the two Gauss points and the RK3 time scheme reach the optimal convergence rate for the unlimited P1 and P2 reconstructions hence the limiting procedure has to be blamed for the accuracy discrepancy.

Figure 3 shows that the optimal convergence rate in L^1 error for P1, MOOD-P1 and MLP methods is achieved since the curves fit very well. On the other hand, the P2 and MOOD-P2 curves are very close and parallel which confirms that MOOD-P2 is an effective third-order method for the L^1 norm. For

Table 5

L^1 and L^∞ errors and convergence orders for the DST on uniform meshes with P1 and P2 methods.

Nb of	P1				P2			
Cells	err_1		err_∞		err_1		err_∞	
20x20	1.334E-01	—	3.227E-01	—	7.130E-02	—	1.729E-01	—
40x40	2.896E-02	2.20	6.593E-02	2.29	9.877E-03	2.85	2.427E-02	2.83
80x80	6.604E-03	2.13	1.408E-02	2.23	1.255E-03	2.98	3.091E-03	2.97
160x160	1.603E-03	2.04	3.310E-03	2.09	1.573E-04	3.00	3.876E-04	3.00
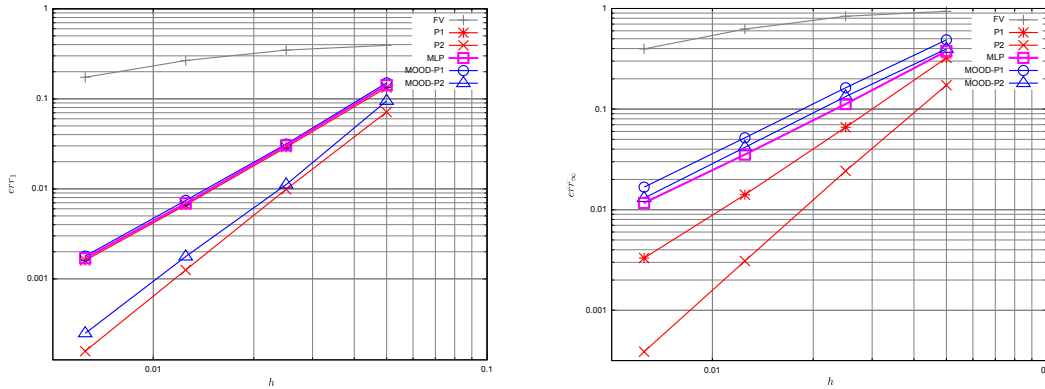
Fig. 3. Convergence curves of err_1(left) and err_∞(right) for the DST on uniform meshes.

the L^∞ norm, none of the limited methods is over the effective second-order while the unlimited P1 and P2 provide an effective second- and third-order respectively. Indeed the strict maximum principle application at extrema is responsible for the L^∞ error discrepancy and we can expect nothing more than a second-order scheme in L^∞ norm, whatever the polynomial degree is when the DMP condition is enforced.

Solid Body Rotation. We employ a 140×140 uniform mesh of square elements in order to compare our results with $100 \times 100 \times 2$ triangular mesh in reference [21]. We display in the left panels of figure 4 three-dimensional elevations while top views of ten uniformly distributed isolines from 0 to 1 are printed in the right panels. We can measure the scheme accuracy by counting the number of isolines outside of the slot since the exact solution isolines would fit the slot shape. The smaller number of isolines outside of the slot is, the more accurate the scheme is. With the MLP reconstruction, we observe three isolines outside while we have only two with the MOOD-P1. At last, the outstanding result is that we have just one isoline outside of the slot with the MOOD-P2 method which proves the great ability of the technique to handle and preserve discontinuities.
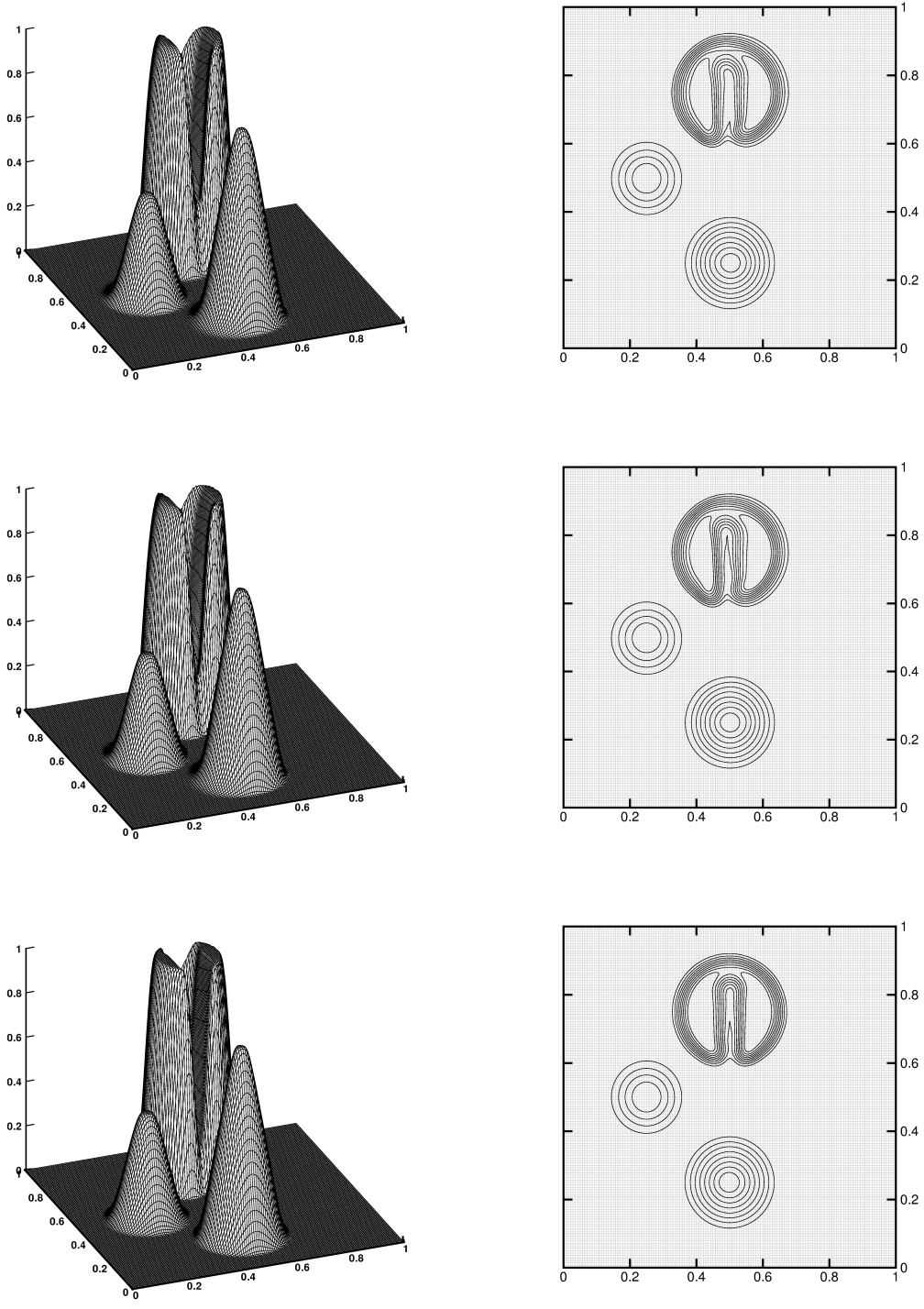
Fig. 4. Results of SBR on a 140x140 uniform mesh. Isolines are from 0 to 1 by 0.1. Top: MLP method — Middle: MOOD-P1 method — Bottom: MOOD-P2 method.
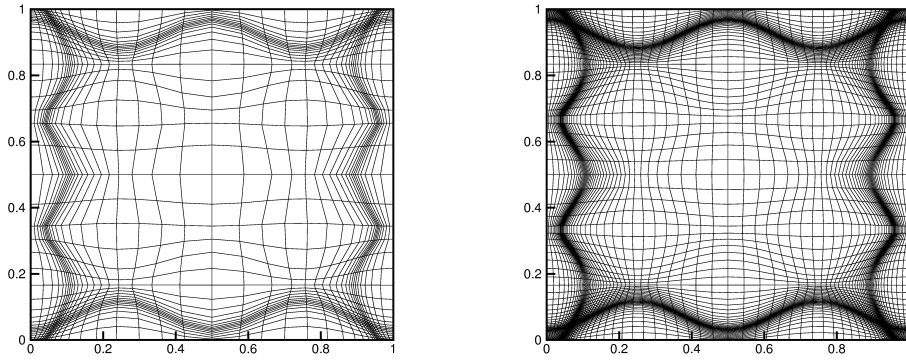
18

Fig. 5. The 40×40 and 80×80 non-uniform meshes for the DST.

6.2.3 Comparison between FV, MLP, MOOD-P1 and MOOD-P2 with EPD_1 strategy on non-uniform meshes

Approximation accuracy is reduced when one employs meshes with large deformations, *i.e.* the elements are no longer rectangular but quadrilateral with large aspect ratios. The present subsection investigates the MOOD method sensitivity to mesh distortion.

To obtain the distorted mesh for the DST, we proceed in two stages. First the following transformation is applied to an uniform mesh

$$x_1 \to \begin{cases} x_1(10x_1^2 + 5x_1 + 1), & \text{if } x_1 \le 0.5, \\ (x_1 - 1)(10(x_1 - 1)^2 + 5(x_1 - 1)) + 1, & \text{elsewhere}, \end{cases}$$

and we operate in the same way with variable x_2.

Then we apply a second transformation

$$x_1 \to x_1 + 0.1|x_1 - 0.5| \cos(6\pi(x_2 - 0.5)) \sin(4\pi(x_1 - 0.5)),$$
$$x_2 \to x_2 + 0.1|x_2 - 0.5| \cos(4\pi(x_1 - 0.5)) \sin(6\pi(x_2 - 0.5)).$$

As an example two non-uniform meshes are given in figure 5. Notice that the shape of domain Ω is preserved by the transformation.

Double Sine Translation. We report in tables 6, 7 and 8 the L^1 and L^∞ errors and convergence rates for FV, MLP, MOOD-P1, MOOD-P2, unlimited P1 and P2 reconstruction methods respectively. At last, we plot in figure 6 the convergence curves for the four methods as well as the convergence curves for the unlimited versions.

We first observe in table 8 an accuracy discrepancy with the unlimited reconstructions since the L^∞ errors are roughly ten times larger for the distorted mesh than for the uniform one given in table 5. Nevertheless, we obtain good effective rates of convergence both in L^1 and L^∞ norm for the P1 and P2

19

Table 6
L^1 and L^∞ errors and convergence rates for the DST on non-uniform meshes with FV and MLP methods.

Nb of	FV				MLP			
Cells	err_1		err_∞		err_1		err_∞	
20x20	4.053E-01	—	9.032E-01	—	3.907E-01	—	8.752E-01	—
40x40	4.038E-01	0.01	9.822E-01	-0.12	1.893E-01	1.05	5.306E-01	0.72
80x80	3.834E-01	0.07	9.486E-01	0.05	4.370E-02	2.11	1.806E-01	1.55
160x160	3.144E-01	0.29	7.825E-01	0.28	9.846E-03	2.15	5.889E-02	1.62

Table 7
L^1 and L^∞ errors and convergence rates for the DST on non-uniform meshes with MOOD-P1 and MOOD-P2 methods.

Nb of	MOOD-P1				MOOD-P2			
Cells	err_1		err_∞		err_1		err_∞	
20x20	3.770E-01	—	8.557E-01	—	3.408E-01	—	7.897E-01	—
40x40	1.599E-01	1.24	4.541E-01	0.91	8.992E-02	1.92	3.222E-01	1.29
80x80	3.892E-02	2.04	1.314E-01	1.79	1.375E-02	2.71	9.199E-02	1.81
160x160	9.170E-03	2.09	3.374E-02	1.96	1.922E-03	2.84	2.483E-02	1.89

Table 8
L^1 and L^∞ errors and convergence rates for the DST on non-uniform meshes with P1 and P2 methods.

Nb of	P1				P2			
Cells	err_1		err_∞		err_1		err_∞	
20x20	3.658E-01	—	8.312E-01	—	FAIL	—	FAIL	—
40x40	1.534E-01	1.25	3.793E-01	1.13	8.328E-02	—	2.135E-01	—
80x80	3.856E-02	1.99	9.760E-02	1.96	1.403E-02	2.57	3.582E-02	2.58
160x160	9.052E-03	2.09	2.643E-02	1.88	1.920E-03	2.87	4.917E-03	2.86

reconstructions. Optimal second-order scheme is achieved for the P1 method and convergence rate is around 2.9 for the P2 reconstruction.
For the L^1 norm, P1, MOOD-P1 and MLP convergence curves fit well hence we get the optimal accuracy with the three methods. In the same way, the P2 and MOOD-P2 are also superimposed which means that MOOD-P2 is optimal with respect to the unlimited case. For the L^∞ norm, MLP method convergence rate is around 1.6 whereas the MOOD-P1, MOOD-P2 and P1 provide a 1.9 convergence rate. Notice that the MOOD-P2 produces more accurate results but does not reach the third-order convergence since it has to respect
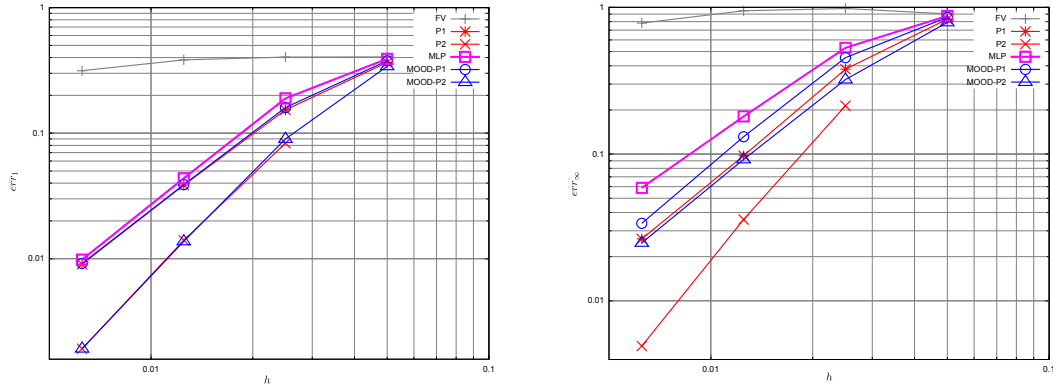
Fig. 6. Convergence curves of err_1(left) and err_∞(right) for the DST on non-uniform meshes.

Table 9

Min and Max for DST on non-uniform meshes with MLP, MOOD-P1 and MOOD-P2.

Nb of	MLP		MOOD-P1		MOOD-P2	
Cells	Min	Max	Min	Max	Min	Max
20x20	-3.740E-02	3.479E-02	-7.168E-02	7.566E-02	-1.376E-01	1.516E-01
40x40	-4.634E-01	4.645E-01	-5.445E-01	5.458E-01	-6.738E-01	6.792E-01
80x80	-8.179E-01	8.204E-01	-8.747E-01	8.743E-01	-9.098E-01	9.079E-01
160x160	-9.433E-01	9.431E-01	-9.655E-01	9.668E-01	-9.752E-01	9.748E-01

a strict DMP property. Finally, table 9 shows that the extrema are better approximated with respect to the exact solution with the MOOD methods than the MLP method, in particular when coarse meshes are employed.

Solid Body Rotation. The mesh deformation presented above is not as relevant for the SBR as for the DST since the solid bodies rotate and do not go through the boundaries. A slight modification of the first step has been done

$$x_1 \rightarrow \begin{cases} x_1(5x_1^2 + 2.5x_1 + 1), & \text{if } x_1 \leq 0.5, \\ (x_1 - 1)(5(x_1 - 1)^2 + 2.5(x_1 - 1)) + 1, & \text{elsewhere.} \end{cases},$$

and we operate in the same way with variable x_2.

The 140×140 non-uniform mesh is visible on the isolines top views. We display in the left panels of figure 7 three-dimensional elevations while top views of ten uniformly distributed isolines from 0 to 1 are in the right panels.

As in the smooth case, MOOD methods perform better than MLP on the distorted mesh. Although they are both second-order methods, we notice that MOOD-P1 gives a clearly better solution than the one computed with MLP, even on the smooth profiles. Moreover the MOOD-P2 result supports the
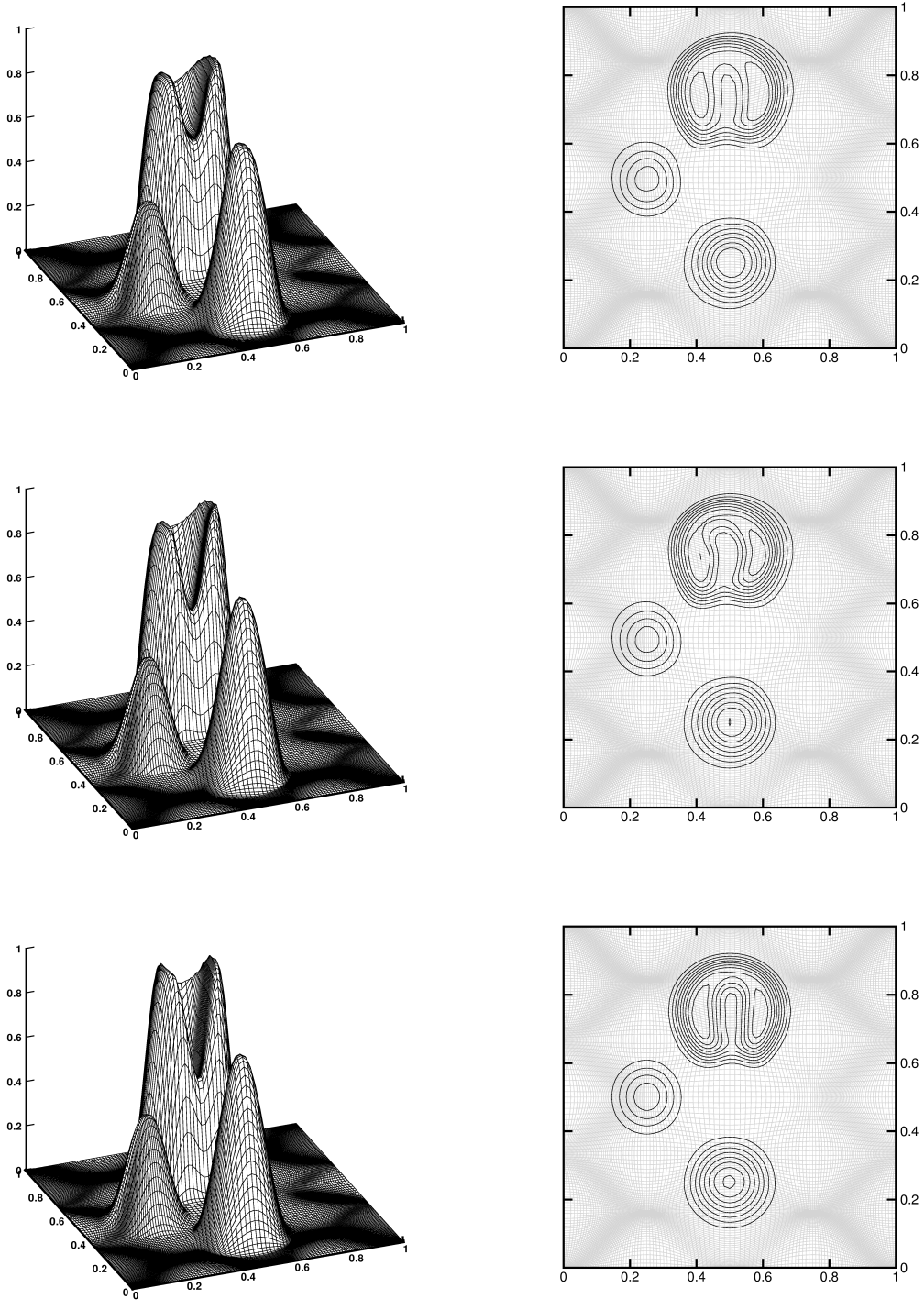
21

Fig. 7. Results of SBR on a 140x140 non-uniform mesh. Isolines are from 0 to 1 by 0.1. Top: MLP method — Middle: MOOD-P1 method — Bottom: MOOD-P2 method.

usefulness of using a third-order method since an important gain in symmetry of the solution is obtained.

7 Numerical results — the Euler case

We now turn to the Euler equations (16) to test the MOOD method. Efficiency, accuracy and stability of the method are investigated on classical tests. In the present article, we use the HLL numerical flux detailed in [26]. Once again comparisons are drawn with the MLP technique proposed in [21]. We apply the MOOD method using the detection strategy presented in Section 5 to each sub-step of the RK3-TVD time discretization.

First the classical 1D Sod shock tube is used to test the ability of MOOD in reproducing simple waves. This test is first run on an uniform mesh and then on a non-uniform one to estimate the gain obtained when using MOOD method. Then we proceed with a 2D Riemann problem proposed by [25] (see also [18]). We conclude the series of tests with two classical references, the Mach 3 wind tunnel with a step problem [21,29] and the double Mach problem [21,29]. These two tests are run with MLP, MOOD-P1 and MOOD-P2 on uniform meshes for comparison purposes with classical results from literature.

7.1 Sod Shock Tube

The one dimensional Sod problem is used as a sanity check for the MOOD method. The computational domain is the rectangular domain $\Omega = [0, 1] \times [0, 0.2]$. The exact solution is invariant in x_2-direction. The interface between the left state $(\rho, u_1, u_2, p) = (1, 0, 0, 1)$ and the right one $(0.125, 0, 0, 0.1)$ is located at $x_1 = 0.5$. Reflective boundary conditions are prescribed. The final time is $t_f = 0.2$.

Uniform mesh. The computational domain is uniformly meshed by 100 cells in the x_1 direction and 10 cells in the x_2 direction. We plot the density and the x_1-velocity at the final time with the exact solution using the MLP, MOOD-P1 and MOOD-P2 methods in figure 8. The curves show a very good agreement between the three methods. The plateau between the contact and the shock is wavy with the MLP method while MOOD produces better constant states. However we observe an undershoot (resp. overshoot) at the tail of the rarefaction with MOOD-P2 for the density (resp. velocity).

Non-uniform mesh. The same simulation is performed on the non-uniform mesh plotted in figure 9. The density and the x_1-velocity solutions at the final time using the MLP, MOOD-P1 and MOOD-P2 methods are also printed in figure 9. All cell values are represented so that the preservation of the 1D
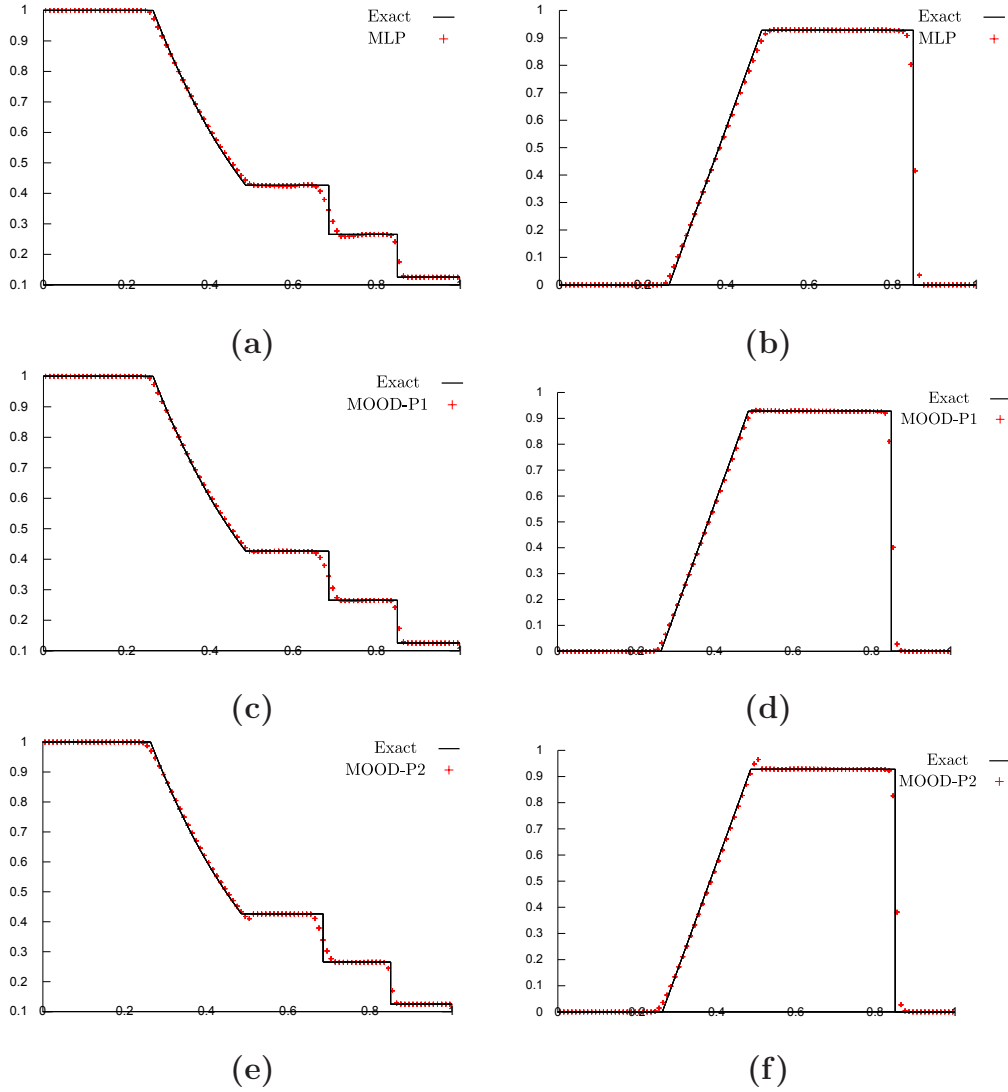
23

Fig. 8. Sod shock tube problem: Density and x_1-velocity solutions on 100×10 uniform mesh for **(a-b)**: MLP — **(c-d)**: MOOD-P1 — **(e-f)**: MOOD-P2.

symmetry in the x_2 direction can be evaluated by the thickness of the points cloud. Clearly the MLP method provides the largest dispersion whereas the MOOD-P2 method manages to better preserve the x_2 invariance. Such a test case suggests that the MOOD method is less sensitive to mesh deformation. As in the uniform case an undershoot at the tail of the rarefaction wave appears for MOOD-P2 method but the solution is genuinely improved by comparison with MLP. The MOOD-P1 is an intermediate case where the dispersion is reduced in comparison with the MLP method but where the MOOD-P2 accuracy is not reached.
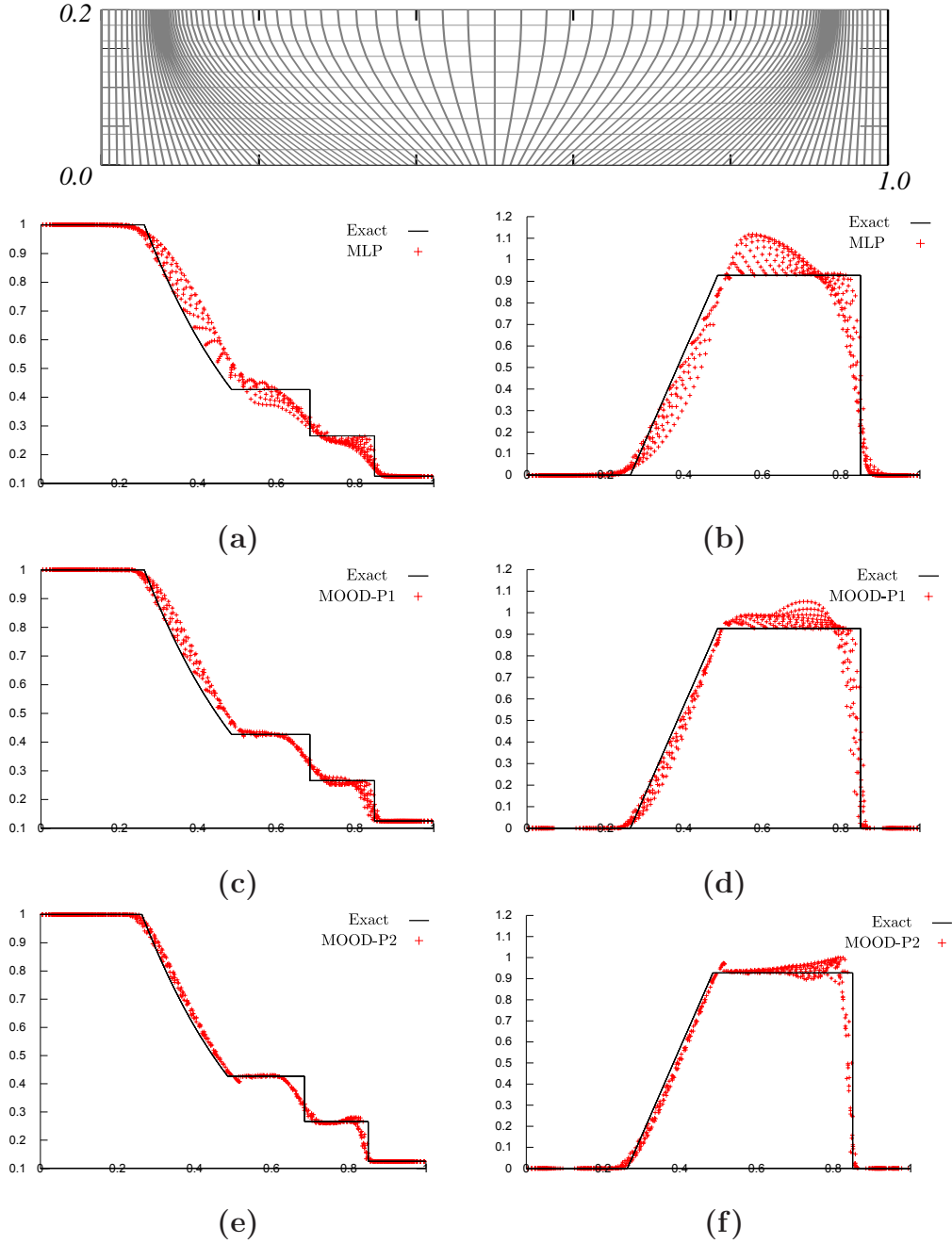
Fig. 9. Sod shock tube problem: Non-uniform 100×10 mesh (Top) — Density and x_1-velocity solutions on the above mesh for **(a-b)**: MLP — **(c-d)**: MOOD-P1 — **(e-f)**: MOOD-P2.

7.2 Four states Riemann problem

We now deal with one of the four states Riemann problem which corresponds to a truly 2D Riemann problem. The computational domain $\Omega = [0,1] \times [0,1]$ is first uniformly meshed by a 100×100 and then by a 400×400 quadrangles grid. The four sub-domains correspond to four identical squares separated by

25

the lines $x_1 = 0.5$ and $x_2 = 0.5$. Initial conditions on each sub-domains are

- for the lower-left domain Ω_{ll}, $(\rho, u_1, u_2, p) = (0.029, 0.138, 1.206, 1.206)$,
- for the lower-right domain Ω_{lr}, $(0.3, 0.5323, 0, 1.206)$,
- for the upper-right domain Ω_{ur}, $(1.5, 1.5, 0, 0)$,
- for the upper-left domain Ω_{ul}, $(0.3, 0.5323, 1.206, 0)$.

Each sub-domain is filled with a perfect gas of constant $\gamma = 1.4$. Outflow boundary conditions are prescribed and the computation is carried out till the final time $t_f = 0.3$. Density at the final time is presented for the three methods in figure 10. For each method on the left side one displays a three-dimensional elevation on the 100×100 mesh while in the right panels 30 isolines are plotted between the minimal density, ρ_m, and maximal one, ρ_M of each method on the 400×400 mesh. The 3D views clearly show that some artificial oscillations on the plateau are generated by the MLP method whereas the MOOD method better preserves the constant states. On the isoline view, we observe that the MOOD-P2 method gives thinner shocks and a finer resolved central peak at $x_1 = x_2 = 0.35$. As expected, this suggests that the MOOD-P2 method is more accurate.

7.3   Mach 3 wind tunnel with a step

The test was initially proposed in [29]. A uniform Mach 3 flow enters in a tunnel which contains a 0.2 unit length step leading to a flow with complex structures of interacting shocks. The wind tunnel is 1 length unit wide and 3 length units long and the step is located at 0.6 length unit from the left-hand side of the domain. At the initial time we consider a perfect gas ($\gamma = 1.4$) with constant density $\rho^0 = 1.4$, uniform pressure $p^0 = 1.0$ and constant velocity $\mathbf{V}^0 = (3, 0)$. Reflective boundary conditions are prescribed for the upper and lower sides as well as in front of the step. An inflow condition is set on the left boundary and an outflow condition on the right one. Numerical simulations are carried out till the final time $t_f = 4$.

We plot a series of figures presenting 30 density isolines for two different uniform meshes on which the three methods are tested. We first consider the situation with coarse mesh using 120×40 cells. Figure 11 represents the density computed with the MLP, the MOOD-P1 and MOOD-P2 methods respectively on top, middle and bottom panels. It is noticeable that the MOOD method results are the most accurate. The shocks are less diffused and we can already observe the contact discontinuity formation of the upper slip line. With the MLP method, we remark that the formation of a triple point at $x_1 = 1.25$ above the step (at a distance of about 0.1) while the junction point should be exactly on the step interface. With the MOOD-P2 method, the triple point is closer to the interface (half the distance with respect to the MLP case).
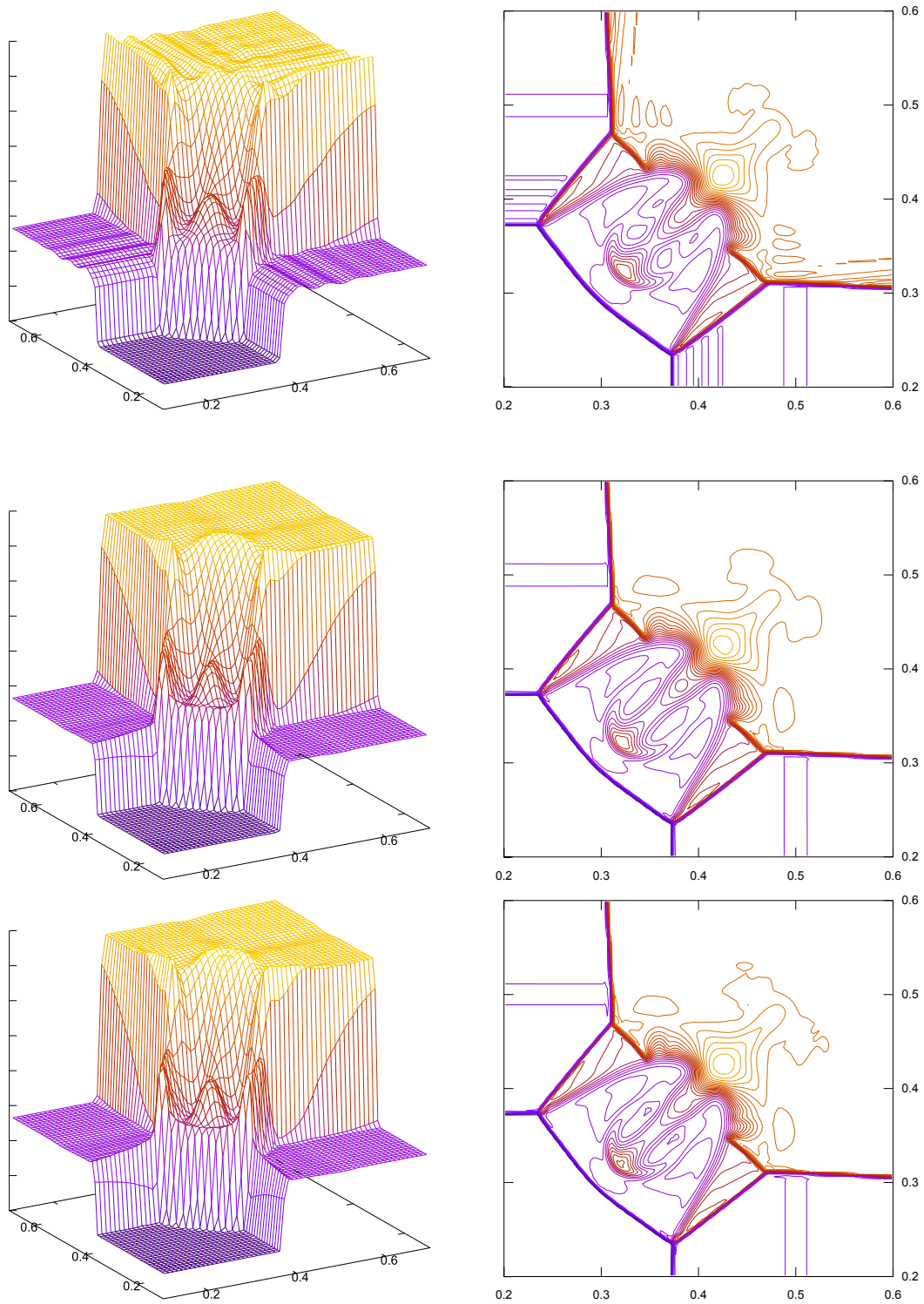
Fig. 10. Density solution to the Four states Riemann problem. On the left 3D views on the 100×100 mesh. On the right top views with 30 isolines between ρ_m and ρ_M on the 400×400 mesh. Top: MLP method $\rho_m = 0.138$ $\rho_M = 1.821$ — Middle: MOOD-P1 method $\rho_m = 0.1377$ $\rho_M = 1.805$ — Bottom: MOOD-P2 method $\rho_m = 0.1379$ $\rho_M = 1.805$.
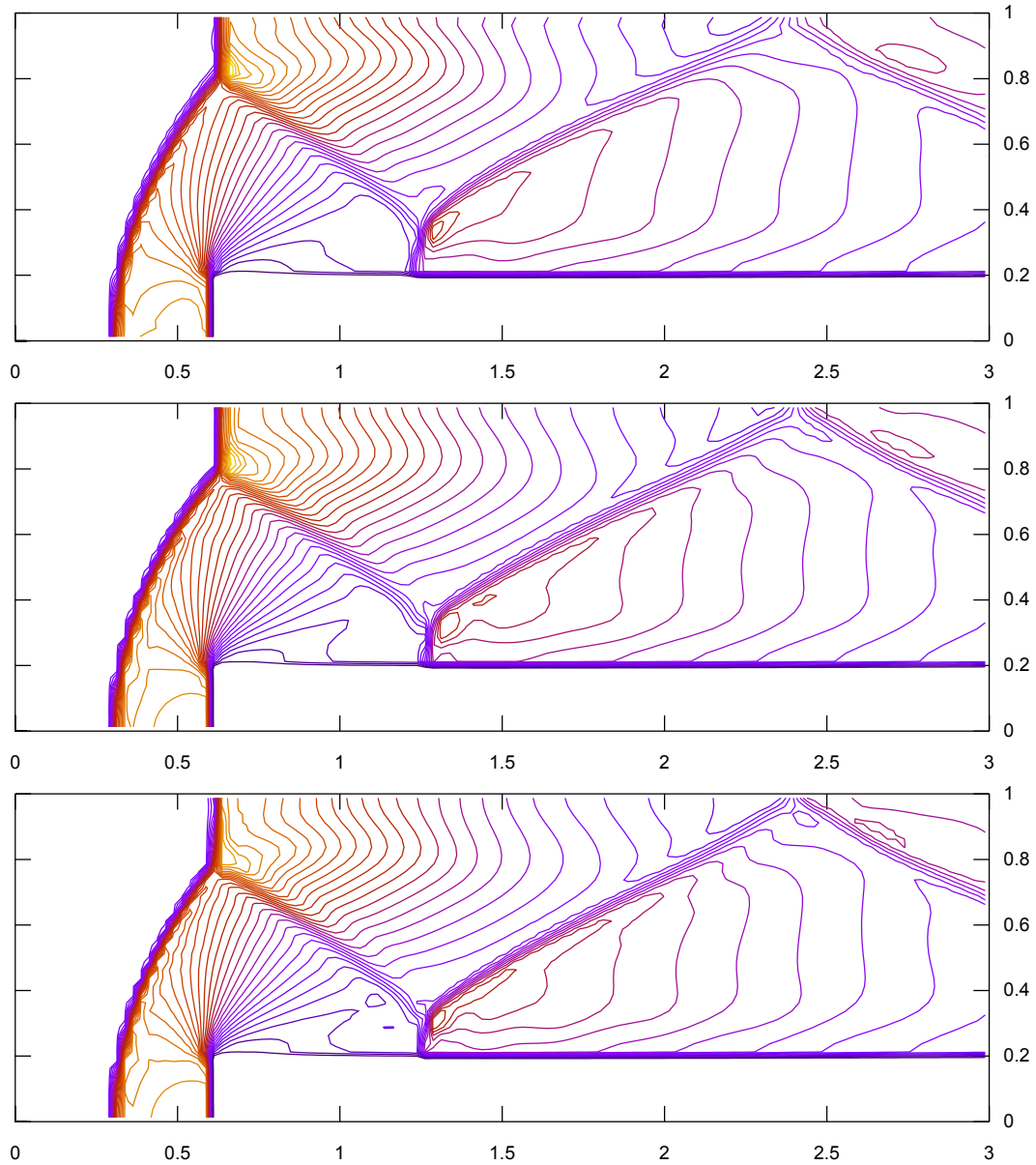
Fig. 11. Mach 3 problem — Density solutions with 30 isolines between ρ_m and ρ_M on a 120×40 uniform mesh. Top: MLP method $\rho_m = 0.5437$ $\rho_M = 6.75$ — Middle: MOOD-P1 method $\rho_m = 0.5589$ $\rho_M = 6.58$ — Bottom: MOOD-P2 method $\rho_m = 0.5358$ $\rho_M = 6.047$.

We plot the density obtained with a finer uniform mesh of 480×160 cells in figure 12. The mesh refinement implies more accurate solutions for any method. Nevertheless MOOD methods still provide the best numerical approximations. However the method does not reveal the Kelvin-Helmholtz instabilities as in [8] as the strict DMP on the density reduces the scheme accuracy along the slip line and consequently increases the numerical dissipation.
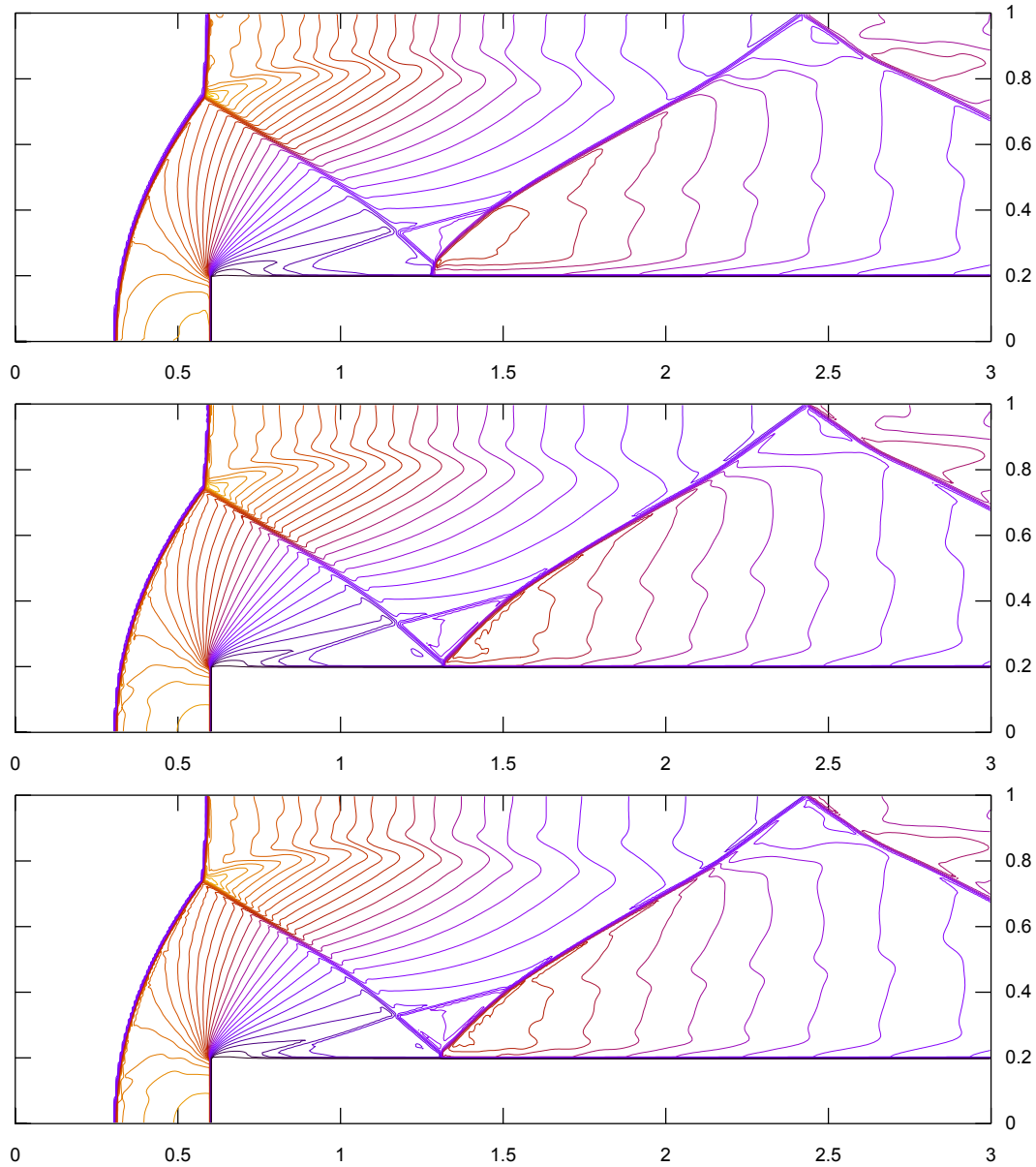
28

Fig. 12. Mach 3 problem — Density solutions with 30 isolines between ρ_m and ρ_M on 480×160 mesh. Top: MLP method $\rho_m = 0.176$ $\rho_M = 6.802$ — Middle: MOOD-P1 method $\rho_m = 0.150$ $\rho_M = 6.483$ — Bottom: MOOD-P2 method $\rho_m = 0.123$ $\rho_M = 6.257$.

7.4 Double Mach reflection of a strong shock

The last problem is the double mach reflection of a strong shock proposed in [29]. This test problem involves a Mach 10 shock which initially makes a 60° angle with a reflecting wall. The air ahead of the shock is at rest and has uniform initial density $\rho^0 = 1.4$ and pressure $p^0 = 1$. A perfect gas with $\gamma = 1.4$ is considered. The reflecting wall lies along the bottom of the domain, beginning at $x_1 = 1/6$. The shock makes a 60 degrees angle with the x_1 axis and extends to the top of the domain at $x_2 = 1$. The short region from $x_1 = 0$ to $x_1 = 1/6$
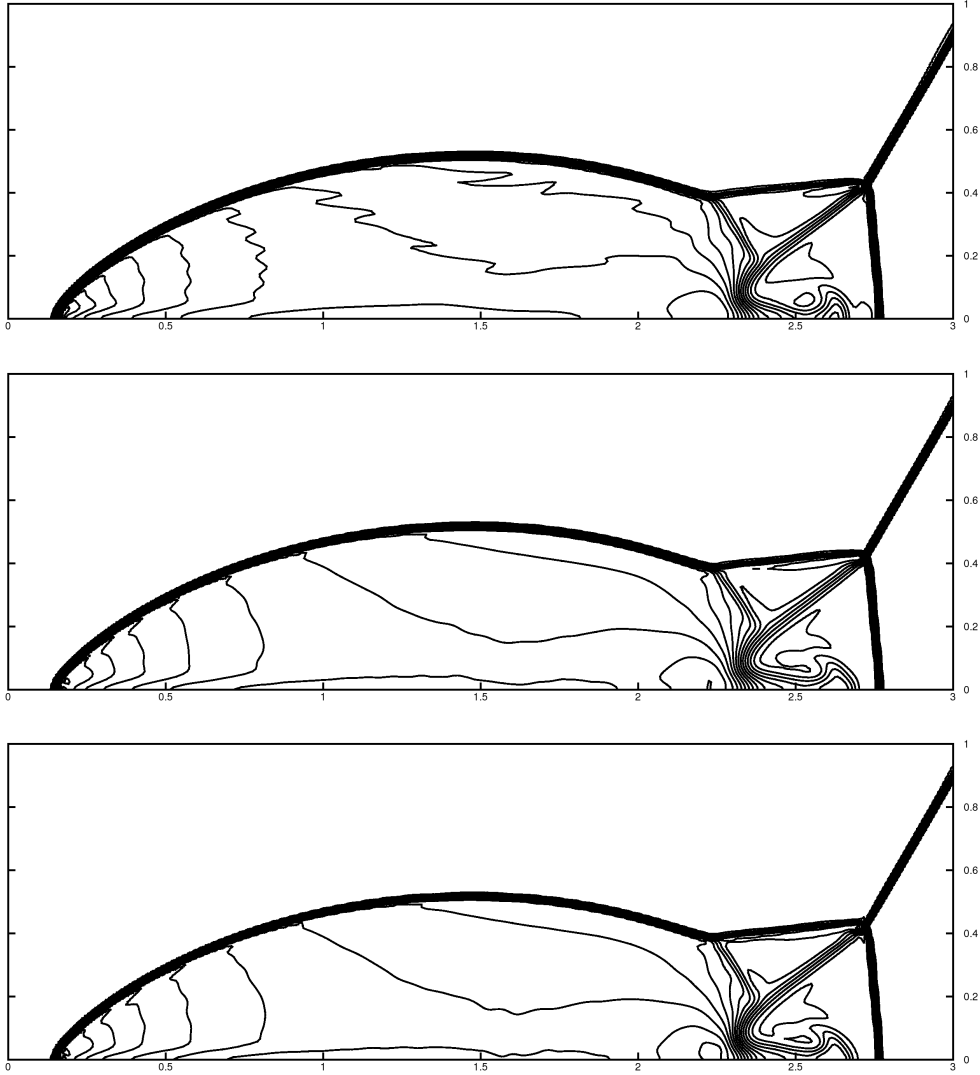
Fig. 13. Double Mach problem on 480×120 — Top: MLP method $\rho_m = 1.40$ $\rho_M = 22.21$ — Middle: MOOD-P1 method $\rho_m = 1.40$ $\rho_M = 20.05$ — Bottom: MOOD-P2 method $\rho_m = 1.40$ $\rho_M = 20.10$.

along the bottom boundary at $x_2 = 0$ is always assigned values for the initial post-shock flow. We prescribe a reflective condition on the bottom part for $x_1 > 1/6$, inflow boundary condition on the left side and outflow condition on the right side. At the top boundary, the boundary conditions are set to describe the exact motion of the Mach 10 flow (see [8]).

First for the three methods, a 30 density isolines top view on the 480×120 uniform mesh using Lax-Friedrich's flux are plotted in figure 13. These results have to be compared to results of figure 12 in [9] and figure 13 in [13]. Then zoomed top views of 50 isolines — between minimal and maximal values, ρ_m and ρ_M respectively, taken over the results of the three methods on a same mesh — of the results obtained with the HLL flux are plotted in figure 14 for the 960×240 uniform mesh on left and for the 1920×480 one on right.

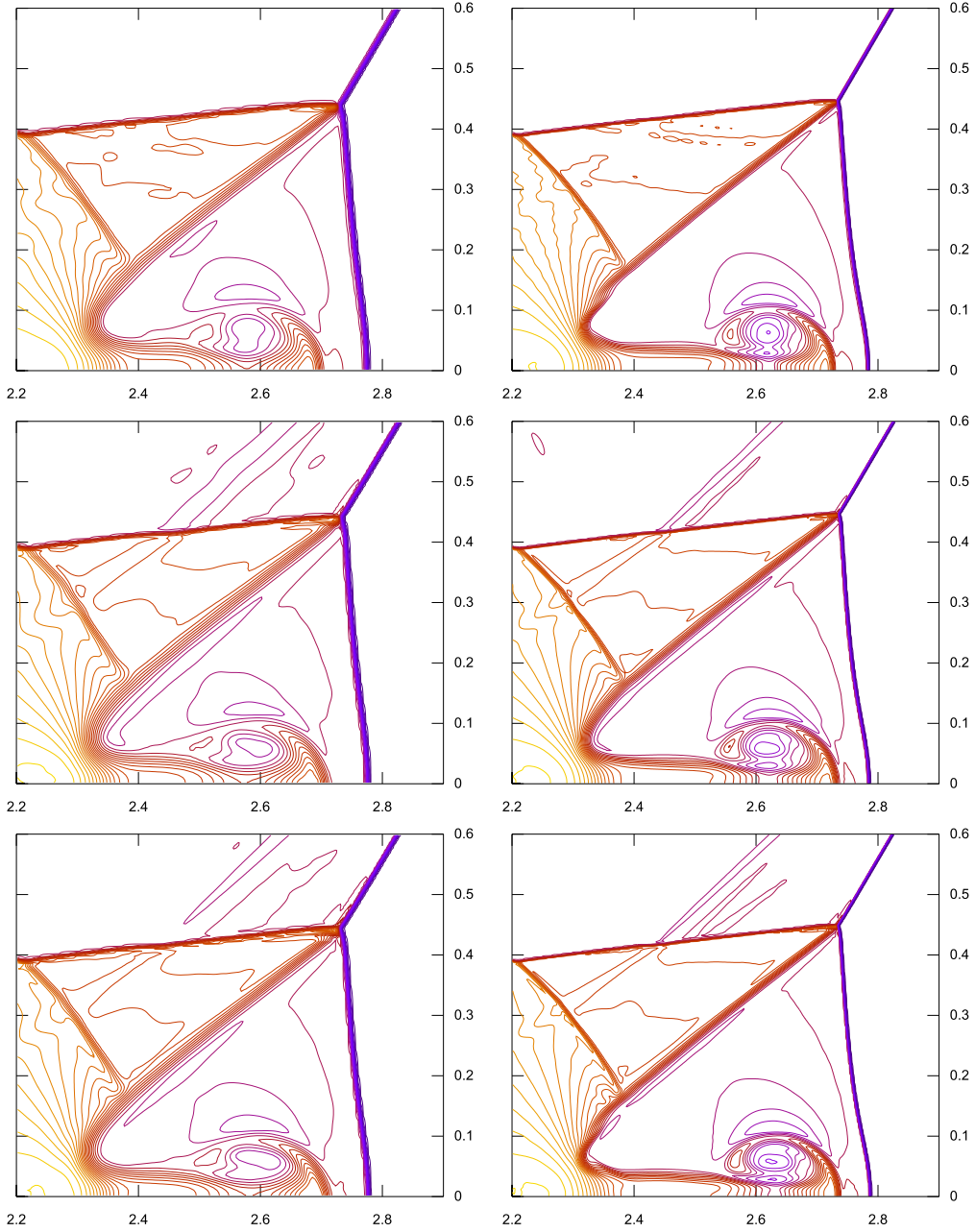The first Mach stem M1 is connected to the main triple junction point with

Fig. 14. Double Mach problem on 960×240 (left) and on 1920×480 (right) — Zoom on the wave interaction zone — Top: MLP method $\rho_m = 1.400$ $\rho_M = 22.400$ on left and $\rho_m = 1.400$ $\rho_M = 22.68$ on right— Middle: MOOD-P1 method $\rho_m = 1.236$ $\rho_M = 22.550$ on left and $\rho_m = 1.216$ $\rho_M = 22.0$ on right — Bottom: MOOD-P2 method $\rho_m = 1.162$ $\rho_M = 22.800$ on left and $\rho_m = 1.146$ $\rho_M = 21.99$ on right.

the incident shock wave and the reflected wave. A slip line is generated from the triple junction point behind the incident shock. A secondary Mach stem M2 also appear and interact with the slip line. As expected, the MOOD-P2 manages to better capture the Mach stem M1 (and M2 when we employ finer meshes) with respect to the two other methods. The slip line corresponds to a contact discontinuity where the jump of tangential velocity may generate

31

Table 10

Computational time ratios between MOOD methods and MLP for different problems.

Method / Problem	MLP	MOOD-P1	MOOD-P2
DST	1	1.1	1.73
SBR	1	1.4	2.65
Sod Shock Tube	1	0.84	1.3
Mach 3 Wind	1	1.08	1.6
Double Mach	1	0.99	1.06
Average	*1*	*1.08*	*1.67*

Kelvin Helmholtz instabilities. Usually, the amount of instabilities measures the numerical diffusion influence [22]: large instabilities derive from small numerical diffusion and the number of plane vortexes in the slip line is a qualitative measure of the scheme diffusivity. In our test, even with the finest mesh, no instability is reported. Indeed, the application of a strict DMP reduces the accuracy of the scheme in the vicinity of the slip line maintaining a too large amount of diffusion. Nevertheless, other choices of detection variables could be investigated to reduce the numerical diffusion of contact discontinuities.

7.4.1 Computational cost comparison between MLP, MOOD-P1 and MOOD-P2

In this last section, we give in table 10 the ratios between MOOD methods computational times and MLP ones. For each test case, computational times are calculated on a given mesh. Numerical experiments show that the ratios are equivalent for finer or coarser meshes.

We recall that these ratios should only be taken as examples because computational times are strongly dependent of implementation and compilation and all runs are carried out on a single core. Table 10 shows that the MOOD-P1 method is slightly more expensive than MLP but gives better results on general meshes. In the scalar case, the difference between ratios of DST and SBR problem are explained by the fact that more iterations during the MOOD procedure, due to more DMP violations, are implied by non-smooth profiles. The MOOD-P2 computational cost is competitive (at most around 2.7 times more expensive than MLP on our numerical experiments) in regard to the observed accuracy improvement, see for instance figures 7 or 9.

8 Conclusion and perspectives

This paper presents a high-order polynomial finite volume method named Multi-dimensional Optimal Order Detection (MOOD) for conservation laws. Contrarily to classical high-order methods MOOD procedure is based on a test of the Discrete Maximum Principle (DMP) after an evaluation of the solution with unlimited polynomials. If the DMP property is not fulfilled then the polynomial degree is reduced and the solution is locally re-evaluated. This procedure is repeated up to satisfaction of the DMP which is always achieved after a finite number of iterations.

There are several important features of MOOD method which have to be compared with classical high-order methods, namely

- The MOOD method is an *a posteriori* limiting process, whereas classical limiting strategies perform an *a priori* limitation.
- The MOOD method computes one and only one high-order polynomial per cell and employs it without any limitation.
- Within the same cell the polynomial degree can be different on each edge.
- The MOOD method ensures the Discrete Maximum Principle (DMP) under the first-order CFL constraint.
- The MOOD method has no restriction to deal with higher polynomial degrees and polygonal meshes.

Two-dimensional numerical results are provided for advection and the Euler equations problems on regular and highly non-regular quadrangular meshes. They clearly show that MOOD method presents some promising good behaviors. The second-order MOOD method is at least equivalent to a second-order multi-dimensional MUSCL method on uniform grids but produces better results on non-uniform ones. A third-order version of MOOD has been shown to be effective on regular and non-regular solutions for a small extra computational effort.

This paper is the first one presenting the MOOD concept and extensions are currently under investigations, as instance the behavior of the MOOD with polynomials of degree greater than two on polygonal meshes.

References

[1] R. Abgrall, On Essentially Non-oscillatory Schemes on Unstructured Meshes: Analysis and Implementation, J. Comput. Phys. 114 (1994) 45–58.

[2] T. J. Barth, Numerical methods for conservation laws on structured and unstructured meshes, VKI March 2003 Lectures Series.

[3] T. J. Barth, D. C. Jespersen, The design and application of upwind schemes on unstructured meshes, AIAA Report 89-0366 (1989).

[4] T. Buffard, S. Clain, Monoslope and Multislope MUSCL Methods for unstructured meshes, J. Comput. Phys. 229 (2010) 3745-3776.

[5] S. Clain, Finite volume L^∞-stability for hyperbolic scalar problems, preprint HAL available at http://hal.archives-ouvertes.fr/hal-00467650/fr/.

[6] S. Clain, V. Clauzon, L^∞ stability of the MUSCL methods, Numer. Math. 116 (2010) 31–64.

[7] I. Christov, B. Popov, New non-oscillatory central schemes on unstructured triangulations for hyperbolic systems of conservation laws, J. Comput Phy. 227 (2008) 5736–5757.

[8] B. Cockburn, C.-W. Shu, The Runge-Kutta Discontinuous Galerkin Method for Conservation Laws V: Multidimensional Systems, J. Comput. Phys. 141 (1998) 199–224. .

[9] O. Friedrich, Weighted Essentially Non-Oscillatory Schemes for the Interpolation of Mean Values on Unstructured Grids, J. Comput. Phys. 144 (1998) 194–212.

[10] A. Harten and S. Osher, Uniformly highorder accurate nonoscillatory schemes I, SIAM J. Num. Anal. 24 (1987) 279–309.

[11] A. Harten, B. Engquist, S. Osher and S. Chakravarthy, Uniformly highorder accurate nonoscillatory schemes III, J. Comput. Phys. 71 (1987) 279–309.

[12] M. E. Hubbard, Multidimensional slope limiters for MUSCL-type finite volume schemes on unstructured grids, J. Comput. Phys. 155 (1999) 54–74.

[13] G.-S. Jiang, C.-W. Shu, Efficient implementation of weighted ENO schemes, J. Comput. Phys. 126 (1996) 202–228.

[14] V. P. Kolgan, Application of the minimum-derivative principle in the construction of finite-difference schemes for numerical analysis of discontinuous solutions in gas dynamics, 1972, Transactions of the Central Aerohydrodynamics Institute, V. 3, N. 6, pp. 68-77, in Russian.

[15] V. P. Kolgan, Finite-difference schemes for computation of three dimensional solutions of gas dynamics and cal- culation of a flow over a body under an angle of attack, 1975, Transactions of the Central Aerohydrodynamics Institute, V. 6, N. 2, 1-6, in Russian.

[16] V. P. Kolgan, Application of the minimum-derivative principle in the construction of finite-difference schemes for numerical analysis of discontinuous solutions in gas dynamics, J. Comput. Phys. 2010, doi: 10.1016/j.jcp.2010.12.033

[17] Randall J. Leveque, High-Resolution Conservative Algorithms for Advection in Incompressible Flow, SIAM J. Num. Anal. 33 (1996) 627-665.

[18] R. Liska, B. Wendroff, Comparison of several difference schemes on 1D and 2D test problems for the Euler equations, SIAM J. Sci. Comput. 25 (2003) 995-1017.

[19] C. F. Ollivier-Gooch, Quasi-ENO Schemes for Unstructured Meshes Based on Unlimited Data-Dependent Least-Squares Reconstruction, J. Comput. Phys. 133 (1997) 6–17.

[20] S. -H. Yoon, C. Kim and K. H. Kim, Multi-dimensional limiting process for three-dimensional flow physics analyses, J. Comput. Phys. 227 (2008) 6001–6043.

[21] J. S. Park, S.-H. Yoon, C. Kim, Multi-dimensional limiting process for hyperbolic conservation laws on unstructured grids, J. Comput. Phys. 229 (2010) 788–812.

[22] J. Shi, Y-T Zhang, C-W Shu, Resolution of high order WENO schemes for complicated flow structures, J. Comput. Phys. 186 (2003) 690–696.

[23] C.-W. Shu, High order weighted essentially nonoscillatory schemes for convection dominated problems, SIAM Review Vol. 51 No 1 (2009) 82–126.

[24] C.-W. Shu, S. Osher, Efficient implementation of essentially non-oscillatory shock-capturing scheme, J. Comput. Phys. 77 (1988) 439–471.

[25] C. W. Schulz-Rinne, J. P. Collins, and H. M. Glaz, Numerical solution of the Riemann problem for two-dimensional gas dynamics, SIAM J. Sci. Comput. 14 (1993) 1394–1414.

[26] E. F. Toro, Riemann Solvers and Numerical Methods for Fluid Dynamics, Springer.

[27] B. Van Leer, Towards the ultimate conservative difference scheme II. Monotonicity and conservation combined in a second order scheme, J. Comput. Phys. 14 (1974) 361–70.

[28] W. R. Wolf , J. L. F. Azevedo, High-order ENO and WENO schemes for unstructured grids, International Journal for Numerical Methods in Fluids, 55 Issue 10 (2007) 917—943.

[29] P. Woodward, P. Colella, The numerical simulation of two-dimensional fluid flow with strong shocks, J. Comput. Phys. 54 (1984) 115–173.